

Evolution of Grain Orientation in front of the Pin during FSW of the 6082-T6 Aluminium Alloy

Zhang Liangliang^{a,*}, Liu Zhiyuan^a, Chen Xiang^a

^aLanzhou City University, School of Bailie Mechanical Engineering, Lanzhou 730070, China.

Received: August 08, 2022; Revised: October 19, 2022; Accepted: October 25, 2022

Friction stir welding (FSW), a new solid-phase connection method, is considered an excellent welding method for aluminium alloys. Grain orientation, grain boundary structure, and texture types in different regions were characterized by a high-resolution electron backscattered diffraction technology. The results revealed that during the welding process, the coarse grains of the base metal are refined, grains in region 1 (600 μm away from the edge of the keyhole) are arranged in a long strip, and the long axis is approximately parallel to the shear direction. The thermal cycle of the welding process causes some grains to recrystallize, further forming a recrystallization (100) [011] rotating-cube texture. The metal in region 2 (100 μm away from the edge of the keyhole) was severely squeezed by the pin, resulting in an increase in the degree of grain breakage in this region, which were mainly equiaxed grains. Due to the eccentric movement of the pin, the (100) [001]-oriented and (110) [001]-oriented grains alternate on the middle layer, forming a banded structure. Plastic deformation and recrystallization occurred in the base metal, within 383 μm in front of the pin, forming a (110) [001] Goss texture and (100) [001] recrystallized cubic texture.

Keywords: 6082-T6 aluminium alloy, friction stir welding, crystal orientation evolution, dynamic recrystallization.

1. Introduction

The 6082-T6 aluminium alloy has advantages of excellent weldability, corrosion resistance, formability, and high specific strength, and it has been widely used in the manufacture of high-speed trains and subway car bodies¹. When using the traditional fusion welding method to weld aluminium alloy, it is easy to produce defects such as pores, welding cracks², and welding-joint softening caused by ageing³. Friction stir welding (FSW), as a new solid-phase connection method⁴, is recognized an excellent welding method for aluminium alloy⁵.

Plastic metal is generated around the pin through forward movements of a high-speed rotating tool, and it is transferred from the front of the pin to the rear under the drive of the pin. Subsequently, it is compressed by the shoulder to form a dense weld⁴. During FSW, plastic-metal flow behaviour and other factors determine the microstructure evolution law and mechanical properties of welded joints⁶. When Fonda⁷ studied the law of the three-dimensional (3D) flow of plastic metal during FSW, they found that metal flow is mainly controlled by shear stress, and this shear stress differs with different weld positions. When polycrystalline materials undergo plastic deformation due to stress, the grains are arranged along a specific direction and appear in a preferred orientation, further forming a certain texture⁸. To further characterize the evolution of grain orientation during FSW, Suhuddin⁹ studied metal flow and microstructure evolution during FSW of 6061 aluminium alloy by using the “stop action” technology¹⁰. Results showed that due to

the shear stress introduced by the pin, a $\{112\} \langle 110 \rangle$ shear texture was formed around the keyhole, while a $\{100\} \langle 100 \rangle$ recrystallized cubic texture was formed in the area far away from the keyhole.

Yanying Hu¹¹ studied the dynamic recrystallization mode during FSW, and they found that the microstructure evolution process can be divided into three main stages. First, when the base metal is subjected to small deformations, strain-induced dislocations occur near the grain boundary, and discontinuous dynamic recrystallization is activated. Subsequently, when the strain and temperature increase, the original grain is elongated. Simultaneously, dislocation proliferation occurs in the grain, and the continuous dynamic recrystallization process begins. Lastly, as the temperature increases further, the high-angle grain boundary mobility of the elongated grains is promoted, which further activates geometric dynamic recrystallization.

Vysotskii¹² studied the plastic deformation behaviour of FSW-welded joints, and the results revealed that there was a small amount of coarse grains in FSW welds. Vysotskiy¹³ found that the plastic deformation of the FSW weld during the stress process was mainly concentrated in the fully recrystallized nugget area, and the elongation after fracture reached 700%. Iuliia¹⁴ increased mechanical impact during FSW. The results revealed that the mechanical impact accelerated the aggregation of S particles at low-angle grain boundaries and further improved the tensile strength of the welds.

During FSW, there are different strain rates at different weld positions, and the size of the stress rate determines the

*e-mail: zll_0715@126.com, zhangll@lzcw.edu.cn

grain orientation. The $A^- \{111\}$ shear texture is formed in the high-strain-rate region, while $B/B^- \{112\}$ and $C \{001\}$ simple shear textures are formed in the low-strain-rate region¹⁵. There are obvious differences in the weld structure along the thickness direction. From the weld surface to the bottom, the grain size gradually decreases¹⁶, and a $\{111\}$ fibre texture is formed on the upper surface of the weld, $\{001\}$ and $\{111\}$ shear textures are formed in the middle layer of the weld, and a $\{110\}$ shear texture is formed at the bottom of the weld¹⁷. The degree of continuous dynamic recrystallization in the thermo-mechanically affected zone on the advancing side(AS) of the weld is less than that on the retreating side(RS), and the volume composition of fully recrystallized grains on the AS is less than that on the RS. There are mainly $\{011\} \langle 211 \rangle$ and $\{221\} \langle 012 \rangle$ textures on the AS, and the texture on the RS is the γ -Fibre ($\langle 111 \rangle // ND$) shear-fibre texture¹⁸. FSW offers the advantages of energy saving and grain refinement¹⁹. By contrast, additive manufacturing technology offers the advantages of high material utilization rate and low cost²⁰. Adopting friction stir welding to realize additive manufacturing by changing the shape of the tool will be one of the future development directions.

Scholars focus on the final structure of the FSW weld or use the “stop action” technology to study the law of evolution of the structure in different areas of the weld, and there is less research on the law of evolution of the structure in front of the pin. This is because the material in front of the pin experiences serious plastic deformations and stores a large amount of strain during FSW. An electron backscattered diffraction(EBSD) sample prepared through the traditional electrolysis method has a low recognition rate. Therefore, research on the law of evolution of the microstructure in front of the pin during FSW is limited. In this study, the triple ion-beam cutter is used to prepare EBSD samples in front of the pin. High-resolution EBSD technology is used to characterize the microstructure in front of the pin, and this closes the gap in research focused on FSW-welded structures. In this study, the “stop action” technique is used to freeze the grain orientation in front of the pin during welding, and EBSD is used to characterize the evolution of grain morphology, grain size, micro-textured components, and grain boundary orientation in this region, thus providing an experimental and theoretical basis for deepening the understanding of the forming mechanism of FSW-welded joints.

2. Materials and Methods

The base material was a 6082-T6 100 mm × 50 mm × 2 mm aluminium alloy, and its composition is shown in Table 1 (The data were obtained by EDS (Oxford Instruments, Oxford, UK)).

During the welding process, a cylindrical shoulder and profiled pin were used to join along the rolling direction. The diameter of the shoulder, diameter of the pin, and length of the pin were 10 mm, 2 mm, and 1.8 mm, respectively, as shown in Figure 1.

The optimum process parameters were as follows: the welding speed was 80 mm/min; the rotation speed was 1200 r/min; the inclination angle of the tool was 3°, and the additional compression of the shoulder was 0.1 mm. After the tool covered a distance of 80 mm, the welding stopped

Table 1. Nominal compositions of the 6082 aluminium alloy employed in this work (wt%).

Si	Mg	Cu	Ti	Fe	Cr	Zn	Al
0.97	0.67	0.07	0.01	0.37	0.01	0.06	Bal

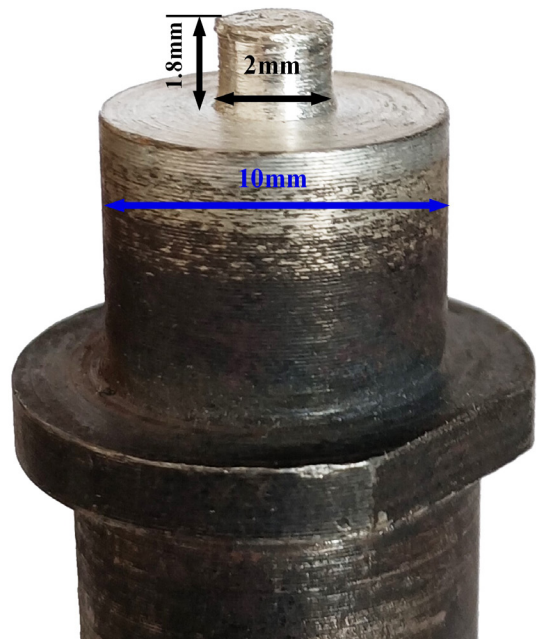


Figure 1. Photo of the welding tool.

immediately, and the dynamic organization was frozen by the ice-water mixture. After the emergency stop, the driving force of the main shaft must be completely removed, but due to inertia, the main shaft continued rotating. This rotational-inertia stage is the transition period, that is, the rotation period when the tool stays at the end of the weld. Prangnell¹⁴ demonstrated that the friction resistance between the shoulder and the surface of the weldment makes the tool stop within 0.1 s. When the rotation speed is 1200 r/min, it is equivalent to the spindle rotating for 2 cycles. Therefore, in this 0.1 s transition period, the shoulder has little effect on its grain orientation. Moreover, the use of the instant emergency-stop cooling technology can retain the dynamic structure in the welding process.

The upper surface of the EBSD sample was coarsely ground with sandpaper, and after mechanical polishing, the surface of the base-metal sample was subjected to electrolytic polishing in a 10% perchloric-acid anhydrous-ethanol solution with a polishing voltage of 20 V, liquid temperature of -20 °C, and a polishing time of 40 s. The sample in front of the pin cut the upper surface with the triple ion-beam cutter to prepare the EBSD sample. The specific EBSD characterization position is shown in Figure 2. Regions 1 and 2 are located on the upper surface of the sample, 600 and 100 μm away from the edge of the keyhole, respectively. Region 3 is located on the middle layer of the sample at the edge of the keyhole. Region 4 is located on the middle layer of the sample, 183 μm away

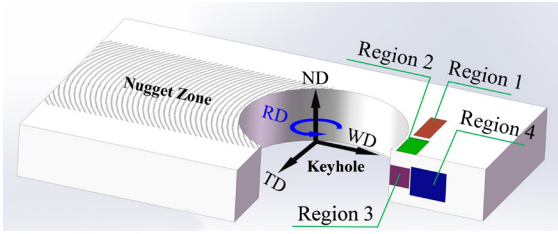


Figure 2. Welding direction and rotation direction of the shoulder and sample location diagram of EBSD maps.

from the edge of the keyhole. A field-emission scanning electron microscope (Quanta 450 FEG) with an EBSD probe (X-Max 80, Aztec) and a Channel 5 orientation analysis system was used to conduct the EBSD test at a voltage of 20 kV. The reference coordinate system obtained during the analysis is shown in Figure 1. In the welding direction (WD), transverse direction (TD), and normal direction (ND), the grain orientations were expressed in the form of $(h\ k\ l)\ [u\ v\ w]$, where $(h\ k\ l)$ was perpendicular to the crystal plane of the ND, and $[u\ v\ w]$ was parallel to the direction of the TD crystal orientation. The grain boundary with a misorientation of $2\sim 15^\circ$ was defined as a small-angle grain boundary, and when it was larger than 15° , it was defined as a large-angle grain boundary. The average grain size was calculated using the equivalent diameter method.

3. Results and Discussion

3.1. Microstructure of the base material

Figure 3 shows the grain morphology and grain-boundary classification diagram of the base metal. The average grain size is calculated according to the equivalent diameter method, and the average grain size of the base metal is $25\ \mu\text{m}$. The grain misorientation is illustrated with a histogram (as shown in Figure 4). The misorientation is close to random misorientation with no obvious preferred orientation.

3.2. Microstructure in front of the pin

A high quality welding joint, with good surface forming, was obtained, as shown in Figure 5a. There is a clear boundary between the nugget zone (NZ) and the heat affected zone (HAZ) at the AS, as shown in Figure 5b. There are equiaxed grains in the centre of the NZ, as shown in Figure 5c. The NZ adjacent to the AS is dominated by the long grain, and the long axis is roughly parallel to the intersection line between NZ and HAZ, as shown in Figure 5d and Figure 5e. Owing to the corrosion resistance of the 6082 aluminium alloy, metallographic specimen corrosion takes a longer time and the corrosion pit appears in localized sections.

3.2.1. Region 1

During FSW, the Shear Direction (SD) is always tangent to the surface of the pin, and the ND of the shear plane is perpendicular to this SD; therefore, there are different SD and Shear Plane Normal (SPN) values in different areas in front of the pin^{21,22}. During the welding process, the pin is aimed at the extrusion of the base metal, and plastic deformation

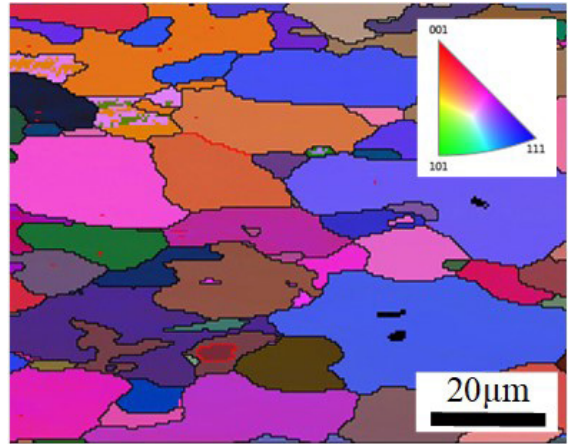


Figure 3. EBSD images of grains and boundaries of the base metal.

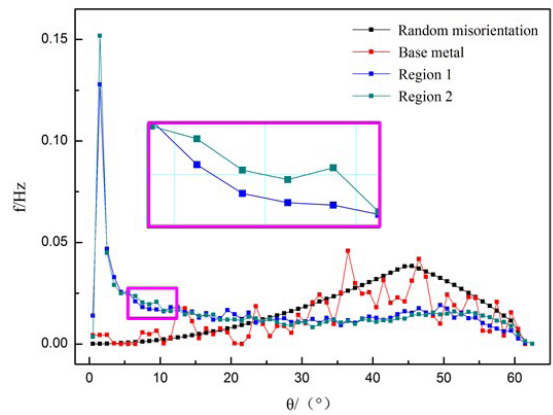


Figure 4. Distribution diagram of misorientation angles between grains.

occurs in the grains, resulting in long-strip grains, as shown in Figure 6(a).

Region 1 is located at the edge of the keyhole, $600\ \mu\text{m}$ away, and it is $2.5\ \text{mm}$ away from the weld centre. Therefore, the included angle between the SD and WD in this region is 47.5° , as shown in Figure 6b. There is no obvious preferred orientation of grains in the 6082-T6 aluminium alloy base metal. During FSW, with the forward movement of the tool, the preferred orientation of the grains appeared $600\ \mu\text{m}$ in front of the pin. According to the detection performed using the high-resolution EBSD technology, this region mainly has $(111)\ [110]$, $(\bar{1}01)\ [121]$, $(114)\ [221]$, and $(100)\ [011]$ rotating cubic textures, as shown in Figure 6.

The stress state of the grain determines the final orientation. For aluminium alloys with a face-centred cubic structure, the maximum shear stress direction is $[110]$ on the (111) plane²³. The appearance of the $(111)\ [110]$ texture in this region indicates that the influence of the pin on the plastic flow of the material is retained, and the shear plane is still parallel to the rotation-direction vector of the pin, and the SD is always parallel to the tangent of the surface of the pin²¹. Compared with the base metal, the grains in this area are obviously refined and arranged in long strips, and the

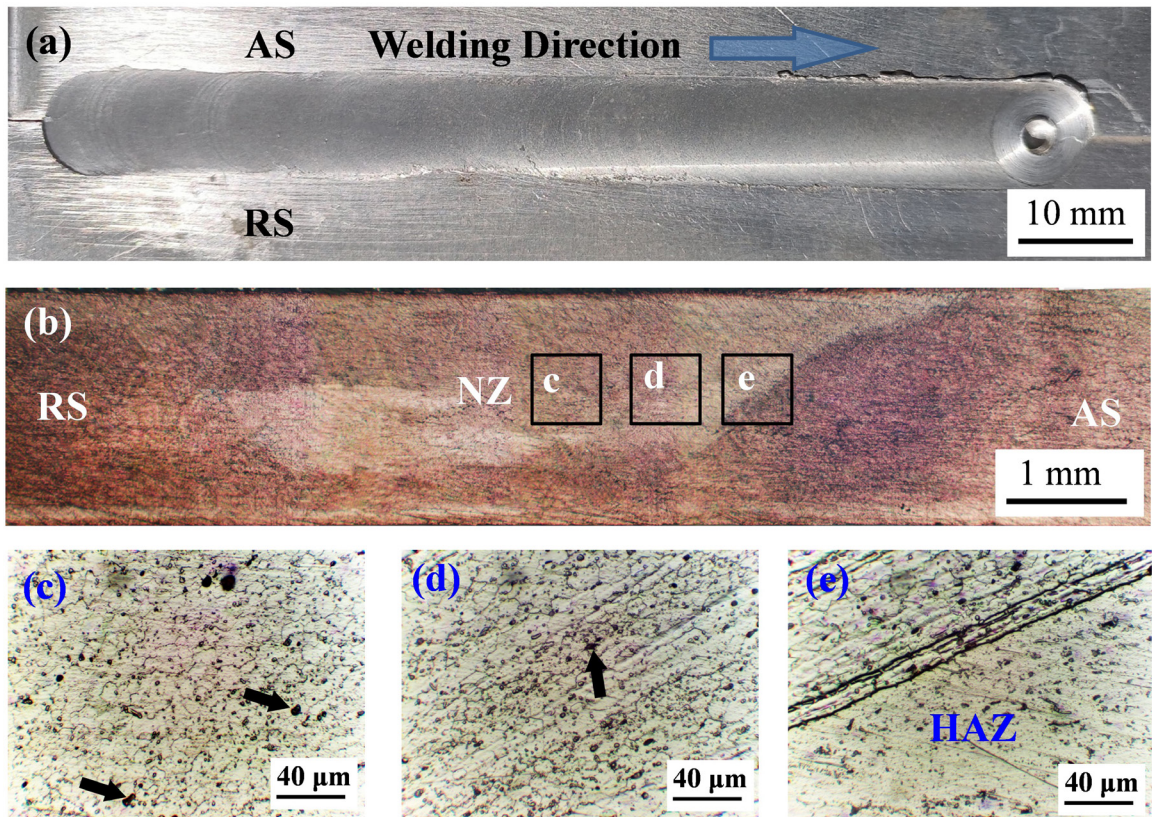


Figure 5. Microstructure of welding joint (a) Weld appearance, (b) Macro metallographic diagram of weld cross section (c) Center of NZ (d) NZ adjacent to AS (e) Junction of NZ and HAZ (The black arrows in Figures 5(c) and (d) indicate the corrosion pits).

long axis of the grains is approximately $10\ \mu\text{m}$. The width is approximately $3\ \mu\text{m}$, and the long axis is approximately parallel to the SD. This is because the tool squeezes the metal material in zone 1, the grains are plastically deformed, and multiple slip systems are activated in the grains simultaneously. During the slip process, the crystals rotate along an axis, which is located in the slip plane perpendicular to the slip direction. Subsequently, the crystals reach the final position along the plane²⁴, and the grains in this region are arranged in a long strip.

The $(\bar{1}01)[121]$ brass texture appears in this region because the $(\bar{1}01)[121]$ orientation is the only stable orientation in the face-centred cubic metal after plastic deformation (especially rolling)²⁴. In the subsequent deformation process, it is not easy to rotate the $(\bar{1}01)[121]$ -oriented grains and change their orientation, and $(\bar{1}01)[121]$ -oriented grains are retained to form a $(\bar{1}01)[121]$ brass texture. Based on the Thompson tetrahedron formed during FSW²⁵, the $(114)[\bar{2}\bar{2}1]$ -oriented grains can easily appear behind the pin, and the appearance of the $(114)[\bar{2}\bar{2}1]$ texture in the upper half of region 1 (region 1.1 shown in Figure 6) shows that the plastic-deformation mode of metal in front of the pin is similar to that behind the pin.

In the lower half of region 1 (region 1.2 shown in Figure 6), a $(100)[011]$ rotational cubic texture is detected. After metal deformation, a certain amount of distortion energy is stored in the grain, and recrystallization occurs

during annealing to form the recrystallization texture. The recrystallization textures of cold-rolled aluminium and aluminium alloy with high deformation are: the cubic texture $(100)[001]$, R texture²⁶, and $(100)[011]$ rotational cubic texture²⁷. The appearance of the $(100)[011]$ rotating cubic texture in region 1 indicates that the deformed grains have undergone recrystallization under the action of the welding thermal cycle, and the recrystallized grains with the $(100)[011]$ rotating cubic orientation are formed due to the rotation of grains. The recrystallization process leads to the fragmentation of long-strip grains, resulting in the necklace arrangement of fine grains.

3.2.2. Region 2

The grain morphology in region 2 is shown in Figure 7. This region is dominated by equiaxed grains. The grains are refined more than those in region 1. The distribution of the orientation difference between grains in the two regions is shown in Figure 4. The composition of small-angle grain boundaries in region 2 is higher than that in region 1. This is the reason a reduction of the distance between the keyhole and the front of the pin increases the extrusion rate of pin in the metal material, which ultimately increases the crushing degree of the coarse grains of the base metal. Through EBSD detection, there are mainly $(111)[\bar{1}10]$, $(10\bar{1})[121]$, and $(100)[011]$ rotating cube textures in region 2, but in the upper half of region 2 (region 2.1 shown in Figure 7), the volume

component of the (100) [011] rotating cube texture is less than that of the lower half of region 2 (region 2.2 shown in Figure 7), as shown in Figure 7a and b. Region 2.1 is closer to the keyhole, and the plastic-deformation degree of the metal

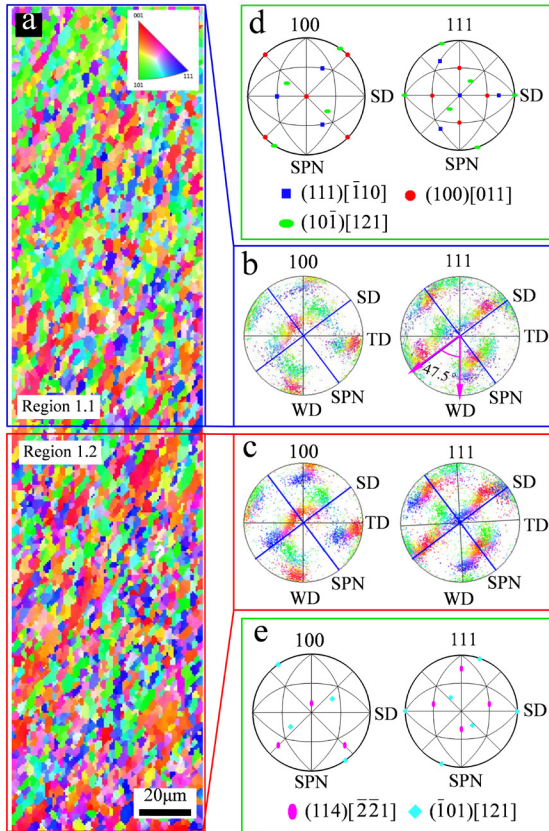


Figure 6. EBSD images of grain morphology and the pole of region 1. (a) grain morphology, (b) 100 and 111 pole figures of region 1.1, (c) 100 and 111 pole figures of region 1.2, and (d)–(e) exact pole figures.

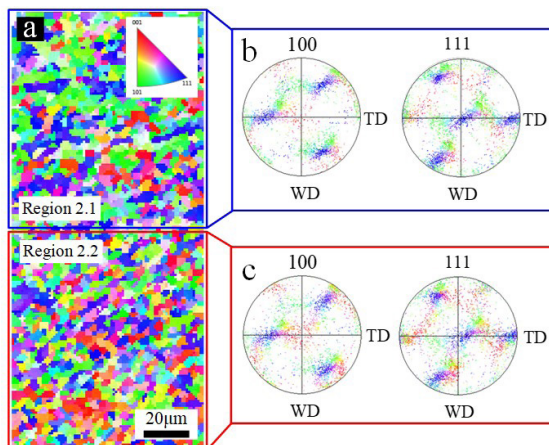


Figure 7. EBSD images of the grain morphology and pole of region 2. (a) Grain morphology, (b) 100 and 111 pole figures of region 2.1, and (c) 100 and 111 pole figures of region 2.2

is higher than that of region 2.2. The stored distortion energy is high. The heat source of the FSW machine is mainly the shoulder, and the maximum temperature occurs in the range of 1/2 to 2/3 of the radius of the shoulder²⁸. The temperature in region 2.1 is lower than that in region 2.2, and the (100) [011] rotating cube texture mainly has a recrystallization texture; therefore, the recrystallization degree in region 2.1 is lower than that in region 2.2. Consequently, the volume component of the (100) [011] rotating cube texture in region 2.1 is less than that in region 2.2.

The volume components of small angle grain boundaries in Region 1 and Region 2 are significantly higher than that of the base metal, as shown in Figure 4. This is primarily because of the plastic deformation of grains due to the extrusion of base metal by the pin during welding, as well as the simultaneous actuation of multiple slip systems in grains, forming subgrains and deformed grains. In the process of stopping, the continuous rotation of the tool under the action of inertia will also affect the small angle grain boundary volume composition in the upper surface metal. The rotation of the tool of inertia is an inevitable limitation of stop-action technology.

3.2.3. Region 3

Region 3 is located on the middle layer of the longitudinal section, and the sampling position is shown in Figure 2. The grain morphology in this area is shown in Figure 8, and there are abnormally grown coarse grains, as indicated by the black arrow in Figure 8. The main forces borne by grain boundaries in the abnormal growth process of grains are: (1) the force driving the decrease in the related grain-boundary energy caused by the decrease in the total grain-boundary area in the system, and (2) the pinning pressure from dispersed second-phase particles. When the hindrance effect of the second-phase particles is greater than or equal to the driving force provided by the grain boundary, the grain growth process stagnates. If the pinning force generated by particle dissolution in local areas of the organization is less than the driving force, individual grains can still continue to grow²⁹. Region 3 is located directly below the shoulder. During the welding process, the shoulder and the upper surface of the workpiece generate heat through friction.

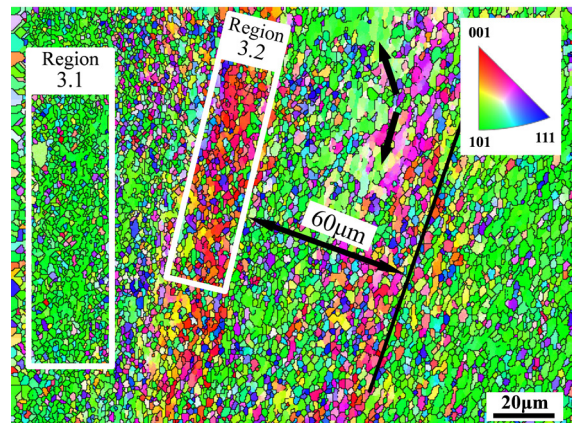


Figure 8. EBSD images of grain morphology of Region 3.

The maximum possible temperature during the welding process is 500 °C³⁰, which makes the MgSi₂ strengthening phase in the 6082-T6 base metal dissolve into the matrix, reduces the pinning force of the strengthening relative to the grain boundary, and leads to the abnormal growth of grains in this zone. It is found that there is a banded structure in this region, and the width of the banded structure is approximately 60 μm. When the welding and rotation speeds are 80 mm/min and 1200 r/min, respectively, the distance travelled by the tool in one revolution is 66 μm, which is equal to the strip width. During the welding process, due to the influence of machining accuracy, the geometric and rotation centres of the tool are not completely coincident; therefore, the pin moves forward in an eccentric manner, and the base metal in front of the pin is extruded intermittently, such that when the base metal is plastically deformed during the welding process, different slip systems are started, resulting in grains with different orientations in front of the pin forming a banded structure. The stereographic projection of grains with different orientations in the banded structure is shown in Figure 9. The results show that there are mainly (110) [001] Goss-oriented grains and (100) [001] cubic-oriented grains in region 3.

Channel 5 software was used to analyse the texture of this region. Table 2 shows the texture types and their volume fractions, calculated by this software. The colours in Figure 10 correspond to the colour types in Table 2. Different colours represent different textures, that is, different Euler angles or orientations. The figure shows that the banded structure is formed by the alternating appearance of (100) [001]-oriented and (110) [001]-oriented grains. The existence of (100) [001]-oriented recrystallized grains indicates that the grains in the base metal in front of the pin not only undergo plastic deformation, but also undergo recrystallization concurrently. There is also a small amount of (111) $\bar{1}10$ -oriented grains at the junction of (100) [001]-oriented and (110) [001]-oriented grains, as shown in Figure 10.

During the welding process, the shear deformation introduced by the pin and shoulder causes dislocation in the grain in front of the pin to pile up and recombine, forming subgrain with (111) $\bar{1}10$ orientation. The subgrain with similar orientation combines into a larger grain through




rotation. During the rotation, the small angle grain boundary becomes a large angle grain boundary, and ‘continuous dynamic recrystallization’³¹ occurs, forming the (111) $\bar{1}10$ shear texture. The formation mechanism of (110) [001] Gaussian texture is similar to that of the (111) $\bar{1}10$ shear texture. Owing to the dislocation density of the (001) [100] cube, the oriented deformed substructure is lower than that of the other oriented substructure. Under the effect of welding thermal cycle, the crystal nucleus grows normally and swallows the non-cube oriented substructure; finally, the recrystallization (001) [100] cube texture appears. This process of forming new grains through nucleation and growth is called ‘discontinuous dynamic recrystallization’³¹. Continuous dynamic recrystallization occurs in front of the pin to form (110) [001] Goss texture and (111) $\bar{1}10$ shear texture. In addition, discontinuous dynamic recrystallization occurs to form (001) [100] cubic texture.

3.2.4. Region 4

Region 4 is located 183 μm in front of the keyhole, and there is still a banded structure within 200 μm to the left of this area, as shown in Figure 11. Stereographic projection is performed on the grains in the banded structure, as shown in Figure 12. In region 4.1, close to the edge of the keyhole, the (110) [001] Goss-oriented grains are mainly present, and in region 4.2 there are (111) $\bar{1}10$ -oriented grains, both of which are grain orientations retained by plastic deformation of the base metal. The right side of this region is the base-metal structure, indicating that the pin and shoulder have no effect on the right side.

The schematic diagram of microstructure evolution in front of the pin is shown in Figure 13. A banded structure appears within 383 μm in front of the pin. In the process

Table 2. Fraction of common textures in region 3.

Colour types	Texture types (h k l) [u v w]	Volume fractions (%)
	(100)[001]	35.7
	(110)[001]	47.4
	(111) $\bar{1}10$	11.3

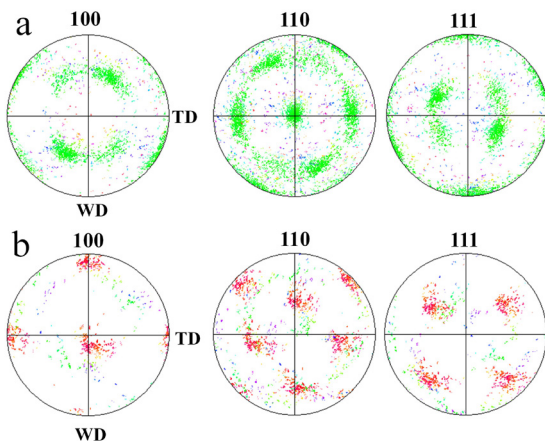


Figure 9. Pole figures for (a) region 3.1 and (b) region 3.2.

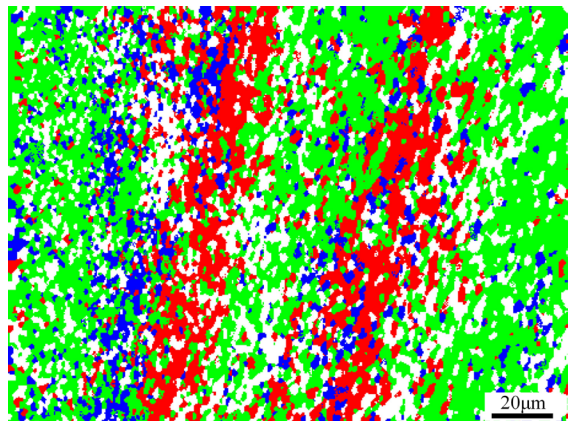


Figure 10. Distribution of grains of various textures.

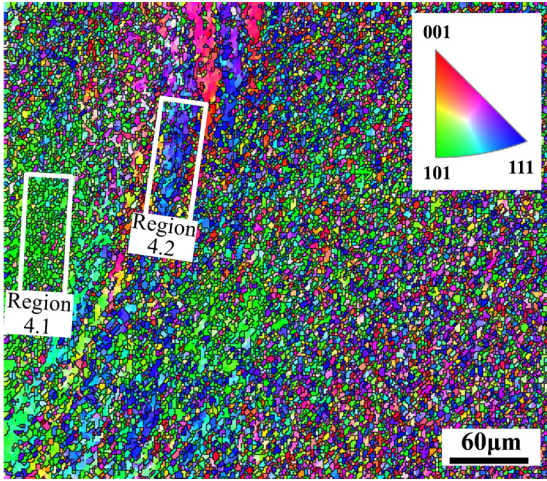


Figure 11. EBSD images of grain morphology in Region 4.

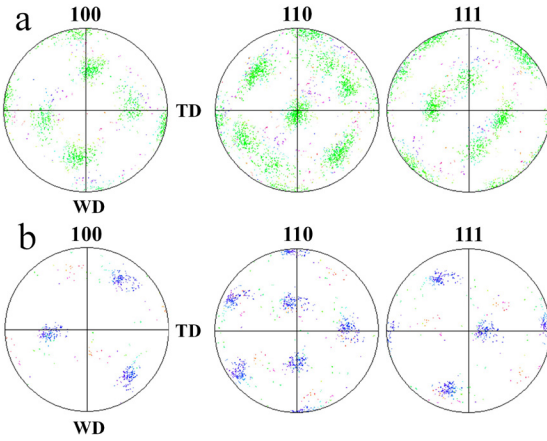


Figure 12. Pole figures for regions (a) and 4.1(b) 4.2.

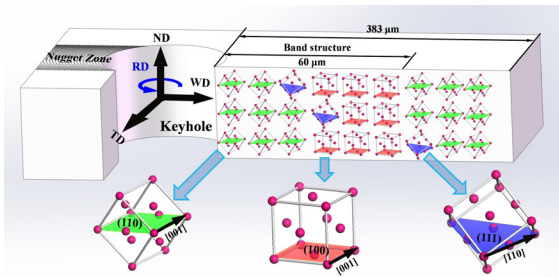


Figure 13. Schematic diagram of microstructure evolution in front of pin.

of FSW, the base metal is transferred from the front of the pin to its rear, and a material flow zone is formed between the pin and the base metal during the transfer process. F.C. Liu³² expressed the mathematical relationship between thickness of material flow zone δ (μm) and the bending forces component through a large number of tests as follows:

$$\delta = 0.38F$$

During the FSW welding of aluminium alloy, the extrusion force of the base metal along the welding direction is approximately 1000 N^{33} . Therefore, the width of the material flow zone during welding is about $380 \mu\text{m}$. In this test, the flowing plastic material was frozen using stop-action technology, and the grain orientation in this area was characterized by EBSD. It was found that only the banded structure appeared in the plastic material flow area of about $380 \mu\text{m}$.

The essence of forming the banded structure is the alternating appearance of (100) [001]-oriented grains and (110) [001]-oriented grains. The pin conducts periodic extrusion on the base metal, and the plasticity turns into a region with low degree, retaining (110) [001]-oriented deformed grains, and high distortion energy is stored in the large deformation region. Under the welding thermal cycle, recrystallization occurs and (100) [001]-oriented grains are formed. A small amount of (111) $[\bar{1}10]$ -oriented deformed grains appears at the junction of the banded structure.

4. Conclusions

- (1) From region 1, where the base metal is $600 \mu\text{m}$ away from the edge of the keyhole, the grains were refined, and the long axis of the grains in region 1 was approximately parallel to the shear direction. In this region, there were mainly (111) $[\bar{1}10]$, $(\bar{1}01)$ $[121]$, (114) $[221]$, and (100) $[011]$ rotating cubic textures; the appearance of the (114) $[221]$ texture indicated that the plastic deformation mode of metal before pin is similar to that after it.
- (2) In region 2, which was $100 \mu\text{m}$ away from the edge of the keyhole, the degree of plastic deformation was higher, which was dominated by fine equiaxed grains, and there were mainly (111) $[\bar{1}10]$, $(10i)$ $[121]$, and (100) $[011]$ rotating cubic textures. The degree of recrystallization in region 2.1 was less than that in region 2.2, resulting in the volume component of the (100) $[011]$ rotating cubic texture in region 2.1 being less than that in region 2.2.
- (3) In region 3 of the longitudinal section in front of the pin, a banded structure was formed due to the alternating occurrence of (100) $[001]$ -oriented and (110) $[001]$ -oriented grains.
- (4) Plastic deformation occurred in the base metal, within $383 \mu\text{m}$ from the pin, and some deformed grains recrystallized, forming a (100) $[001]$ recrystallized cubic texture; beyond $383 \mu\text{m}$, the pin and shoulder had no significant effect on the base metal.

5. Acknowledgments

This work was supported by the Science and Technology Program of Gansu Province (No. 21JR7RA545), Lanzhou talent innovation and Entrepreneurship Project (No. 2021-RC-51), the Gansu Provincial Department of Education: Young Doctor Fund Project (2022QB-174), and the Gansu Provincial Department of Education: Innovation Fund Project (2022A-139).

6. References

- Feng Q, Jun Z, Hou Z, Niu X. Research on microstructure and properties of double-sided friction stir welding joint of 6082 aluminum alloy. *Trans China Weld Inst.* 2021;42(2):75-80.
- Nong Q, Xie YD, Jin CY. Research status and perspectives of welding process for aluminum alloy. *Hot Working Technology.* 2013;42(9):160-2.
- Qi N, Xie Y. Soften and strengthen mechanism of welded joints of Al-Mg-Si 6061 alloy. *Work Technol.* 2012;41(9):148-50.
- Luan G, Qiao G. High-effective solid-phase new welding technology FSW. *Electr Weld Mach.* 2005;35(9):8-13.
- Threadgill PL, Leonard AJ, Shercliff HR, Withers PJ. Friction stir welding of aluminium alloys. *Int Mater Rev.* 2009;54(2):49-93.
- Wu C, Hao S, Lei S. Numerical simulation of heat generation heat transfer and material flow in friction stir welding. *Chin Shu Hsueh Pao.* 2018;54(2):265-77.
- Fonda RW, Rowenhorst DJ, Knipling E. 3D material flow in friction stir welds. *Metall Mater Trans, A Phys Metall Mater Sci.* 2019;50(2):655-63.
- Mao W, Ping Y, Leng C. *Cailiao zhigou fenxi yuanli yu jiance jishu.* Beijing: Metallurgical Industry Press; 2008. p. 4-5.
- Suhuddin U, Mironov S, Sato YS, Kokawa H. Grain structure and texture evolution during friction stir welding of thin 6016 aluminum alloy sheets. *Mater Sci Eng A.* 2010;527(7-8):1962-9.
- Pragnell PB, Heason CP. Grain structure formation during friction stir welding observed by the 'stop action technique'. *Acta Mater.* 2005;53(11):3179-92.
- Hu Y, Niu Y, Zhao Y, Yang W, Ma X, Li J. Friction stir welding of CoCrNi medium entropy alloy: recrystallization behaviour and strengthening mechanism. *Mater Sci Eng A.* 2022;848:143361.
- Vysotskii I, Malopheyev S, Mironov S, Kaibyshev R. Deformation behavior of friction stir welded Al-Mg-Mn alloy with ultrafine-grained structure. *Mater Charact.* 2022;185:111758.
- Vysotskiy I, Kim K, Malopheyev S, Mironov S, Kaibyshev R. Superplastic behavior of friction-stir welded Al-Mg-Sc-Zr alloy in ultrafine-grained condition. *Trans Nonferrous Met Soc China.* 2022;32(4):1083-95.
- Morozova I, Królicka A, Obrosova A, Yang Y, Doynov N, Weiß S, et al. Precipitation phenomena in impulse friction stir welded 2024 aluminium alloy. *Mater Sci Eng A.* 2022;852:143617.
- Liu XC, Sun YF, Nagira T, Ushioda K, Fujii H. Strain rate dependent micro-texture evolution in friction stir welding of copper. *Materialia.* 2019;6:100302-7.
- Zhou L, Xu F, Yu M, Jiang Z, Zhao D, He W, et al. Microstructural characteristics and mechanical properties of friction-stir-welded CuSn6 tin bronze. *J Mater Eng Perform.* 2019;28(7):4477-84.
- Meshram MP, Tamboli RR, Kodli BK, Yebaji SG, Dey SR. Texture analyses of friction stir welded austenitic stainless steel AISI-316L. *Adv Mater Process Technol.* 2018;4(2):244-54.
- Moradi MM, Jamshidi Aval H, Jamaati R, Amir Khanlou S, Ji S. Microstructure and texture evolution of friction stir welded dissimilar aluminum alloys: AA2024 and AA6061. *J Manuf Process.* 2018;32:1-10.
- Li Y, Li F, Wu Z, Qin F. Influence of technological parameters on microstructure and mechanical properties of FSW AZ31 magnesium alloy. *Trans China Weld Inst.* 2020;41(4):31-7.
- Tian G, Wang W, Chang Q, Ren Z, Wang X, Zhu S. Research progress and prospect of wire and arc additive manufacture. *Mater Rep.* 2021;35(23):23131-41.
- Fonda RW, Knipling KE, Bingert JF, Reynolds AP, Tang W, Colligan KJ, et al. Texture development in aluminum friction stir welds. *Mater Process Texture.* 2011;16(4):228-36.
- Gratecap F, Girard M, Marya S, Racineux G. Exploring material flow in friction stir welding: tool eccentricity and formation of banded structures. *Int J Mater Form.* 2012;5(2):99-107.
- Hu GX, Cai X, Rong YH. *Fundamentals of materials science.* Shanghai: Shanghai Jiao Tong University Press; 2010. p. 158-9.
- Yong S, Zhao P, Liu Q. Microstructure and tensile property inhomogeneity of commercial 7055-T7951 aluminum alloy thick plate by hot rolling. *Rare Met Mater Eng.* 2020;4(12):4199-206.
- Sato YS, Kokawa H, Ikeda K, Enomoto M, Hashimoto T, Jogan S. Microtexture in the friction-stir weld of an aluminum alloy. *Metall Mater Trans, A Phys Metall Mater Sci.* 2001;32(4):941-8.
- Yang ZY, Zhang J, Guo XB. Research progress on aluminum alloy texture and test analysis. *J Netshape Form Eng.* 2013;5(6):1-6.
- Chen H, Bai J, Lu R, Lin JB. Microstructure and texture of new ultra-strength aluminum alloy during hot deformation and annealing processes. *Chinese J Nonferrous Met.* 2014;24(9):2243-9.
- Du YF, Bai JB, Tian ZJ, Zhang Y. Investigation on three-dimensional real coupling numerical simulation of temperature field of friction stir welding of 2219 aluminum alloy. *Trans China Weld Inst.* 2014;35(8):57-70.
- Pu J, Sun W, Hui Z. Effects of postweld heat treatment on microstructure and mechanical properties of 6063-T6 aluminum alloy friction stir welding joints. *Foundry Technol.* 2022;43(4):270-5.
- Yang Z, Li W, Li Z, Liu X, Li W. Effect of multifacets stirring pin on material flow behavior for friction stir welding. *Chinese J Mech Eng.* 2022;58(6):81-90.
- Huang K, Logé RE. A review of dynamic recrystallization phenomena in metallic materials. *Mater Des.* 2016;111:548-74.
- Liu FC, Nelson TW. In-situ material flow pattern around probe during friction stir welding of austenitic stainless steel. *Mater Des.* 2016;110:354-64.
- Lambiase F, Paoletti A, Di Ilio A. Forces and temperature variation during friction stir welding of aluminum alloy AA6082-T6. *Int J Adv Manuf Technol.* 2018;99:337-346.